

Numerical aspects of an algorithm for the Eulerian simulation of two-phase flows

Paulo J. Oliveira^{1,*},[†] and Raad I. Issa^{2,‡}

¹*Departamento de Engenharia Electromecânica, Universidade da Beira Interior, 6201-001 Covilhã, Portugal*

²*Department of Mechanical Engineering, Imperial College of Science, Technology and Medicine,
London SW7 2BX, U.K.*

SUMMARY

It is often the case that the numerical simulation of two phase flows leads to a number of difficulties associated with the solution algorithms utilized. Those difficulties manifest themselves as an impossibility to converge the iterative solution process, typical of the finite-volume pressure-correction methods, and are particularly persistent in cases with phase segregation (complete, or almost complete, separation of one phase from the other) and with fine meshes. A number of effective measures to overcome such problems are here proposed and tested, encompassing: (1) modification of the momentum equations formulation in a way that avoids singularity as volume fractions (α) tend to zero; (2) bounding of the volume fractions during the iterative algorithm in a way that enforces the physical limits, $\alpha \geq 0$ and ≤ 1 ; (3) symmetric treatment of some terms in the equations, and consistent formulation of cell-face fluxes in order to prevent numerical-induced oscillations. Copyright © 2003 John Wiley & Sons, Ltd.

KEY WORDS: two-phase flow; numerical method; Eulerian formulation

1. INTRODUCTION

Numerical modelling of two phase flows using the Eulerian approach is one in which both phases are treated as interpenetrating continua and suitably averaged momentum equations are solved for both [1]. In this study we examine, from a numerical perspective, the behaviour of a typical finite-volume algorithm for the solution of the Eulerian equations for two phase flow. By ‘typical’ we mean pressure-based, iterative algorithms similar to that described in previous work [2], which in many ways descends from the early IPSA algorithm of Spalding [3]. Recent representative applications of that type of algorithm are given in the work of References [4, 5].

* Correspondence to: P. J. Oliveira, Departamento de Engenharia Electromecânica, Universidade da Beira Interior, 6201-001 Covilhã, Portugal.

[†] E-mail: pjpo@ubi.pt

[‡] E-mail: r.issa@ic.ac.uk

Contract/grant sponsor: Fundação para a Ciência e Tecnologia (FCT); contract/grant number: FMRH/BSAB/68/98

Experience with iterative two-phase flow algorithms (for example Reference [2]) has invariably led to numerical problems, especially when there is segregation of the phases or when recirculation zones occur. In practical terms the outcome is the impossibility to converge the iterative-like procedure used to solve the sets of discretized equations. Often convergence is hindered due to the inability to solve the equations to the prescribed tolerance in only a few problematic cells of the mesh, but the solution is otherwise achieved in most of the computational domain. Lack of robustness is also observed when the computational grid is refined.

The purpose of this work is to investigate some of the key numerical issues which affect the robustness of two-phase algorithms and to devise and test various procedures designed to improve algorithm performance. In particular, the following issues have been studied:

- Behaviour of the velocity field for each phase as the volume fractions go to zero. The standard formulation for the momentum equations becomes singular in that limit, so the resulting velocities can fluctuate widely in the regions where volume fractions tend to vanish. This causes numerical problems, especially at the boundary between regions of segregated phases.
- Boundedness of the volume fraction field, especially as the volume fraction tends to one of its physical limits (zero or one). This issue is related to the choice of equations solved to obtain the volume fractions, as will be discussed in the paper.
- Behaviour of the algorithm with mesh refinement. One of the important requirements of a generally applicable algorithm is ‘robustness’, when fine computational meshes are used to obtain numerically resolved solutions.
- Capability of the algorithm to handle phase segregation.

The proposed remedies have been tested and verified for several test cases which exhibit the flow features above and the results of these tests are presented.

2. DIFFERENTIAL EQUATIONS

In this section the standard form of the averaged momentum equations comprising the Eulerian two-fluid model for two-phase flows are given first, and then the steps required to obtain a working set of equations, after division of each by its volume-fraction, are explained. The final form of the governing equations are listed at the end of the section.

2.1. Basic governing equations

The basic averaged equations are those representing conservation of mass and momentum for each phase k (c for continuous and d for dispersed):

$$\frac{\partial}{\partial t} \alpha_k + \nabla \cdot \alpha_k \mathbf{u}_k = 0 \quad (1)$$

$$\frac{\partial}{\partial t} \rho_k \alpha_k \mathbf{u}_k + \nabla \cdot \rho_k \alpha_k \mathbf{u}_k \otimes \mathbf{u}_k = \nabla \cdot \alpha_k \mathbf{T}_k + \rho_k \alpha_k \mathbf{g} + \mathbf{M}_k \quad (2)$$

The averaging procedure and the resulting equations are by now relatively well established [1] although some differences may arise due to the detailed treatment of the interphase terms. In Equations (1) and (2), \mathbf{u} is a phase averaged velocity, \mathbf{g} is the acceleration of gravity, α is a volume fraction, and both phases are assumed to have a constant density ρ . The total stress tensor is decomposed into an isotropic pressure term and an effective (molecular + turbulent) deformation stress as:

$$\mathbf{T}_k = -p_k \boldsymbol{\delta} + \boldsymbol{\tau}_k \quad (3)$$

where $\boldsymbol{\delta}$ is the identity tensor. The interface momentum transfer term can be decomposed into drag (D), virtual mass (VM) and an interface-average stress contribution (I), denoted by a corresponding superscript, as

$$\mathbf{M}_k = \mathbf{M}_k^D + \mathbf{M}_k^{VM} + \mathbf{M}_k^I \quad (4)$$

with

$$\mathbf{M}_k^D = C_f [\alpha_k \hat{\alpha}_k (\hat{\mathbf{u}}_k - \mathbf{u}_k) - \eta_k \nabla \alpha_k] \quad \left(C_f = \frac{3}{4} \frac{\rho_c C_D u_r}{d_p} = \frac{18 \mu_c f(Re_p)}{d_p^2} \right) \quad (5)$$

$$\mathbf{M}_k^{VM} = \rho_c C_{VM} \alpha_k \hat{\alpha}_k \left(\frac{D \hat{\mathbf{u}}_k}{Dt} - \frac{D \mathbf{u}_k}{Dt} \right) \quad (6)$$

$$\mathbf{M}_k^I = \int_{A_i} \mathbf{T}_{ki} \cdot \mathbf{n}_k \, da = -\mathbf{T}_{ki} \cdot \nabla \alpha_k = p_{ki} \nabla \alpha_k - \boldsymbol{\tau}_{ki} \cdot \nabla \alpha_k \quad (7)$$

where the symbol $\hat{\cdot}$ denotes the other phase and index i refers to interface (of area A_i). Other interface forces are known to arise and be significant in some circumstances, such as lift or history forces, but their effect on the numerical behaviour of the algorithm has not been considered here. Furthermore, since the objective was to study numerical aspects of the solution procedure, simple models have been used for the phasic interactions, although they assume the usual forms which lead to numerical difficulties. The drag was assumed to follow the standard curve (e.g. Reference [1]) for drag around a sphere of diameter d_p , namely $C_D = (24/Re_p) f(Re_p)$ with the function $f(Re_p) = 1 + 0.15 Re_p^{0.687}$, where the particle Reynolds number is defined in terms of the relative velocity $u_r = |\mathbf{u}_d - \mathbf{u}_c|$ and the continuous phase viscosity μ_c , as $Re_p = \rho_c u_r d_p / \mu_c$. Also [6, 7], the instantaneous drag gives rise to a turbulent drag term, proportional to the eddy diffusivity ($\eta_k = v_k^t / \sigma_\alpha = \mu_k^t / \rho_k \sigma_\alpha$, with $\sigma_\alpha = 0.71$) in Equation (5).

2.2. Alternative form of the equations

As mentioned earlier, in the limit of $\alpha_k \rightarrow 0$, the momentum equation for phase k becomes singular. Division of the momentum equations by α_k leads to well-behaved velocity fields in the limit of vanishing velocity of the other phase; in the absence of flow-induced accelerations, the velocity of either phase will then tend to the corresponding ‘terminal velocity’. If the momentum Equations (2) are expressed in non-conservative form (by

differentiating the convection terms; see e.g. Reference [8]) and then divided by α_k we obtain

$$\begin{aligned} \rho_k \frac{Du_k}{Dt} = & -\nabla p_k + \nabla \cdot \boldsymbol{\tau}'_k - \frac{2}{3} \rho_k \nabla k_k + \rho_k \mathbf{g} - \mathcal{A}_k \frac{\nabla \alpha_k}{\alpha_k} + \hat{\alpha}_k C_f (\hat{\mathbf{u}}_k - \mathbf{u}_k) \\ & + \hat{\alpha}_k \rho_c C_{VM} \left(\frac{D\hat{\mathbf{u}}_k}{Dt} - \frac{D\mathbf{u}_k}{Dt} \right) \end{aligned} \quad (8)$$

where

$$\mathcal{A}_k = -(p_{ki} - p_k) + C_f \eta_k \quad (9)$$

is a dispersion coefficient. In Equation (8) it is assumed that $\tau_{ki} = \tau_k$, but a difference between the average phase stress and its interfacial average could be included. The effective stress is linearly related to the strain rate via a Boussinesq relationship, with the effective viscosity being the sum of molecular and turbulent contributions (to be obtained from the k - ε turbulence model), $\mu^{\text{ef}} = \mu + \mu^t$. In arriving at Equation (8) the stress was decomposed as

$$\boldsymbol{\tau}_k = \boldsymbol{\tau}'_k - \frac{2}{3} \rho_k k_k \boldsymbol{\delta} \quad (10)$$

where k is the turbulence kinetic energy, and:

$$\boldsymbol{\tau}'_k = \mu_k^{\text{ef}} (\nabla \mathbf{u}_k + \nabla \mathbf{u}_k^T - \frac{2}{3} \nabla \cdot \mathbf{u}_k \boldsymbol{\delta}) \quad (11)$$

The normal turbulent stress is written separately (using the stress deviator $\boldsymbol{\tau}'$) because it is an important factor for phase dispersion and may be subjected to specific numerical treatment.

It is noted that the simplifications leading to Equation (8) were possible because the interface forces (drag, Equation (5), and virtual mass, Equation (6)) were assumed to be proportional to the product of both volume fractions, $\alpha_k \hat{\alpha}_k$. Not all authors make that assumption, but there are physical arguments to justify it. In fact, the drag acting on a phase k (first term on right-hand side of Equation (5)) should vanish when the ‘other’ dragging phase is not present ($\hat{\alpha}_k \rightarrow 0$), and also when there is nothing to drag, that is $\alpha_k \rightarrow 0$. Such ‘symmetric’ feature of the drag coefficient with respect to either phase was recognised as early as 1975 by Harlow and Amsden [9] (see their Equation (6)); later, in 1987, Spalding [10] used a similar symmetry in his development of a two-fluid turbulence model.

A more quantitative argument can be given. Consider a steady upflow of bubbles in a liquid (hence $\rho_c > \rho_d$; $\Delta \rho \equiv \rho_c - \rho_d$) under fully developed conditions, when the pressure gradient balances the effects of drag and buoyancy. The momentum equations reduce to (from Equations (2) and (5)):

$$0 = -\alpha_c \frac{\partial p}{\partial x} + \alpha_c \alpha_d C_f (u_d - u_c) - \alpha_c \rho_c g$$

$$0 = -\alpha_d \frac{\partial p}{\partial x} + \alpha_c \alpha_d C_f (u_c - u_d) - \alpha_d \rho_d g$$

If the first equation is multiplied by α_d , the second by α_c , and the two are subtracted, we obtain for the relative velocity ($u_r \equiv u_d - u_c$):

$$C_f u_r = g \Delta \rho$$

For a linear Stokes drag (low Re_p , so $f(Re_p) \rightarrow 1$ in Equation (5)) this equation yields $u_r = g \Delta \rho d_p^2 / 18 \mu_c$, and for non-linear drag (high Re_p , constant drag coefficient C_D) $u_r = \sqrt{\frac{4}{3} d_p g \Delta \rho / \rho_c C_D}$. So we see that the relative velocity is independent of the concentration (α_d or α_c), as it should unless a refined drag modelling was employed. If the drag force were proportional to $\alpha_d C_f$ and not to $\alpha_c \alpha_d C_f$, then the relative velocity in this simplified situation would be proportional to α_c (or $\sqrt{\alpha_c}$ at high Re_p), a clearly incorrect result.

A consequence of the present manipulation is that the only problematic term remaining, when $\alpha_k \rightarrow 0$, is the interfacial term proportional to $\nabla \alpha_k / \alpha_k$. It is required that the gradient of α goes to zero faster than α_k , as $\alpha_k \rightarrow 0$. Numerically, it is easy to discretise this term in such a way that no division by a zero α_k will occur (it suffices to represent the α in the denominator of $\nabla \alpha / \alpha$ by the average of cell face α 's). This is obviously a much simpler question than the original problem of a singular equation $0 = 0$. Physically, the fact that this modelled term remains problematic after division by α_k might be an indication that some of the model assumptions are incorrect and require further study, a matter that goes beyond the present purposes (which are purely numerical).

2.3. Special symmetric treatment of terms

In arriving at the final form of the momentum equations, from Equation (8), two terms deserve special attention so that the resulting equations remain symmetric in relation to either phase. We deal first with the gravity term and then with the normal stress term.

It will generally be assumed that the same static pressure acts in both phases, $p_k = p$. The gravity terms in the above equations are usually written in terms of a buoyancy term appearing solely in the dispersed phase equation, after subtracting the weight of the continuous phase from the static pressure. This manipulation leads to modified pressure gradient and body-force terms of the form (prior to division by the volume fraction):

continuous phase :

$$-\alpha_c \nabla \bar{p} \tag{12}$$

dispersed phase :

$$-\alpha_d \nabla \bar{p} - \alpha_d g \Delta \rho \quad (\text{with } \Delta \rho = \rho_c - \rho_d)$$

where $\bar{p} = p + \rho_c g z + \text{constant}$ (z is the direction vertically upwards and g is the magnitude of gravity). When there is no reason to treat one of the phases differently from the other, such as in separated flow regimes (stratified flow, for example), it is better to use a symmetric treatment and define the modified pressure as:

$$\nabla \bar{p} = \nabla p - g \rho_m \quad (\text{with } \rho_m = \alpha_c \rho_c + \alpha_d \rho_d) \tag{13}$$

A manipulation similar to that above leads now to modified pressure gradient and body-force terms of the form (prior to division by the volume fraction):

continuous phase :

$$-\alpha_c \nabla \bar{p} + \alpha_d \alpha_c \mathbf{g} \Delta \rho \quad (14)$$

dispersed phase :

$$-\alpha_d \nabla \bar{p} - \alpha_d \alpha_c \mathbf{g} \Delta \rho$$

The advantage of this new modified pressure is that \bar{p} will not suffer any change of slope across a stratified flow.

In what relates to the turbulent normal stress term (the $2/3 \rho \nabla k$ terms in Equation (8)) they can be included into a modified pressure in a symmetric way similar to that for the gravity terms above. The original momentum equation has terms of the form:

$$-\alpha_k \nabla p - \frac{2}{3} \alpha_k \rho_k \nabla k_k$$

where it is assumed that the densities ρ_k are constant. Define the modified pressure as

$$\nabla \bar{p} = \nabla p + \frac{2}{3} (\alpha_c \rho_c \nabla k_c + \alpha_d \rho_d \nabla k_d) \quad (15)$$

where the turbulent kinetic energies of the continuous and dispersed phases are k_c and k_d , respectively. These are related to each other in the turbulence model employed in this work by $k_d = C_k k_c$. Then the relevant terms in the equations become:

continuous phase :

$$-\alpha_c \nabla \bar{p} - \alpha_d \alpha_c \frac{2}{3} \nabla (\rho_c k_c - \rho_d k_d) \quad (16)$$

dispersed phase :

$$-\alpha_d \nabla \bar{p} + \alpha_d \alpha_c \frac{2}{3} \nabla (\rho_c k_c - \rho_d k_d)$$

2.4. Final equations

After inserting the symmetric treatment just explained for the gravity and normal stress into the momentum equations, we arrive at the following working form of the various governing equations.

Momentum equation for the continuous phase

$$\begin{aligned} \rho_c \frac{D\mathbf{u}_c}{Dt} = & -\nabla p + \nabla \cdot \boldsymbol{\tau}'_c - \frac{2}{3} \alpha_d \nabla (\rho_c k_c - \rho_d k_d) + \alpha_d \mathbf{g} \Delta \rho + \mathcal{A}_c \frac{\nabla \alpha_d}{\alpha_c} \\ & + \alpha_d C_f (\mathbf{u}_d - \mathbf{u}_c) + \alpha_d \rho_c C_{VM} \left(\frac{D\mathbf{u}_d}{Dt} - \frac{D\mathbf{u}_c}{Dt} \right) \end{aligned} \quad (17)$$

Momentum equation for the dispersed phase:

$$\begin{aligned} \rho_d \frac{D\mathbf{u}_d}{Dt} = & -\nabla p + \nabla \cdot \boldsymbol{\tau}'_d + \frac{2}{3} \alpha_c \nabla (\rho_c k_c - \rho_d k_d) - \alpha_c \mathbf{g} \Delta \rho - \mathcal{A}_d \frac{\nabla \alpha_d}{\alpha_d} \\ & + \alpha_c C_f (\mathbf{u}_c - \mathbf{u}_d) + \alpha_c \rho_c C_{VM} \left(\frac{D\mathbf{u}_c}{Dt} - \frac{D\mathbf{u}_d}{Dt} \right) \end{aligned} \quad (18)$$

with: $\mathcal{A}_c = \mathcal{A}_d = C_f v^t / \sigma_\alpha$ (here it is assumed that $p_{ki} = p_k$).

Continuity equation for the continuous phase:

$$\frac{\partial}{\partial t} \alpha_c + \nabla \cdot \alpha_c \mathbf{u}_c = 0 \quad (19)$$

Continuity equation for the dispersed phase:

$$\frac{\partial}{\partial t} \alpha_d + \nabla \cdot \alpha_d \mathbf{u}_d = 0 \quad (20)$$

Equation of phase compatibility:

$$\alpha_c + \alpha_d = 1 \quad (21)$$

Turbulence modelling is not the issue under study here, hence the equations governing the transport of turbulent kinetic energy ($k \equiv k_c$) and its dissipation rate ($\varepsilon \equiv \varepsilon_c$) [6, 7] are merely stated below. They are:

$$\rho_c \frac{Dk}{Dt} = \nabla \cdot \frac{\mu^t}{\sigma_k} \nabla k + (G - \rho_c \varepsilon) + S_k \quad (22)$$

$$\rho_c \frac{D\varepsilon}{Dt} = \nabla \cdot \frac{\mu^t}{\sigma_\varepsilon} \nabla \varepsilon + \frac{\varepsilon}{k} (C_1 G - C_2 \rho_c \varepsilon) + S_\varepsilon \quad (23)$$

where G is the generation of turbulence kinetic energy and the various constants in the model took standard values: $\sigma_k = 1$; $\sigma_\varepsilon = 1.3$; $C_1 = 1.44$; $C_2 = 1.92$. It should be noted that the original transport equations for k and ε have been divided by α_c following a procedure similar to that for the momentum equations. The source terms accounting for the presence of a dispersed phase and its influence upon the continuous phase turbulence are:

$$S_k = 2k\alpha_d C_f (C_i - 1) + C_f \frac{v^t}{\sigma_\alpha} \frac{\nabla \alpha_d}{\alpha_c} \cdot \mathbf{u}_r \quad (24)$$

for the kinetic energy, where the mean slip velocity is $\mathbf{u}_r = \mathbf{u}_d - \mathbf{u}_c$, and

$$S_\varepsilon = 2C_3 \varepsilon \alpha_d C_f (C_i - 1) \quad (25)$$

for the dissipation rate. In these turbulence modulation terms, the most important contribution is related to the covariance or interaction coefficient defined as $C_i = \overline{\mathbf{u}'_d \cdot \mathbf{u}'_c} / \overline{\mathbf{u}'_c \cdot \mathbf{u}'_c}$, where \mathbf{u}' are velocity fluctuations. It is noted that the $(C_i - 1)$ -term in these dispersed-phase-related terms should be treated implicitly if $C_i < 1$ (case of solid particles in a gas); otherwise (gas bubbles

in a liquid, $C_i > 1$), it should be left on the right-hand side of the equations. The dispersed phase turbulent kinetic energy and viscosity are related to the continuous phase ones by means of response functions:

$$k_d = C_k k_c \quad \text{and} \quad \nu_d^t = C_\nu \nu_c^t$$

with

$$\nu^t \equiv \nu_c^t = C_\mu k_c^2 / \varepsilon \quad (C_\mu = 0.09), \quad \mu_c^{\text{ef}} = \mu_c + \rho_c \nu_c^t \quad \text{and} \quad \mu_d^{\text{ef}} = \rho_d (\nu_d + \nu_d^t).$$

In this work we have used $C_\nu = 1$, $C_i = 1$, $C_3 = 0$ (no turbulent modulation terms) and C_k followed an expression given by Reference [6]:

$$C_k = C_t^2, \quad \text{with} \quad C_t = \frac{3 + \beta}{1 + \beta + 2\rho_d/\rho_c}, \quad \beta = \frac{t_\varepsilon}{t_p} \left(1 + 2\frac{\rho_d}{\rho_c} \right)$$

where t_ε is a time scale of the large eddies (typically $t_\varepsilon = C_\varepsilon k / \varepsilon$, with $C_\varepsilon = 0.4$) and t_p is the 'particle' relaxation time ($t_p = (\rho_d / C_f)(1 + C_{VM}\rho_c/\rho_d)$, with $C_{VM} = 0.5$).

3. DISCRETISED EQUATIONS

In this section the discretized form of the governing equations, which is based on a standard finite-volume method, is given. The methodology developed to ensure that the volume fractions remain bounded is then presented. This is a key point of the work and one that has received little attention in the past, albeit being essential to ensure robustness of the numerical method.

3.1. Momentum equations and fluxes

A non-staggered mesh arrangement is utilized, following previous work [2]. All variables (denoted ϕ) are stored at the centre of the control volumes over which the governing equations are integrated, resulting in sets of linearized algebraic equations of the form

$$a_P \phi_P = \sum_F a_F \phi_F + S_\phi \quad (26)$$

where a_F and a_P are coefficients accounting for convection and diffusion influences, from any surrounding cell F onto the cell P in question, and S are source terms containing all other influences (see e.g. References [11, 12]). The various systems of equations like (26) are then solved sequentially with conjugate gradient methods for linear-equation sets. All this is standard matter and the classical reference for the kind of finite volume method we use is the book by Patankar [11].

Following the finite volume method, the implicitly discretised cell-centered momentum equations (at cell P), with implicit treatment of drag and virtual mass, is written in simplified 1-D fashion as

$$\begin{aligned} a_P u_P = & \sum_F a_F u_F - B_P [\Delta p]_P - V_P \mathcal{A}_P \frac{[\Delta \alpha]_P}{\alpha_P} + \hat{\alpha}_P C_f \hat{u}_P V_P \\ & + \left(\frac{\rho' V}{\delta t} \right)_P u_P^0 + S'_u + \rho_c \hat{\alpha}_P C_{VM} \sum_F \hat{\alpha}_F' (\hat{u}_P - \hat{u}_F) \end{aligned} \quad (27)$$

with the central coefficient evaluated as

$$a_P = \sum_F a_F + \left(\frac{\rho' V}{\delta t} \right)_P + \hat{\alpha}_P C_f V_P \quad (28)$$

where each neighbour coefficient is composed by diffusion and virtual-mass corrected convection contributions

$$a_F = a_F^{\mathcal{D}} + a_F^{\mathcal{C}} \quad (29)$$

All the other terms on the right-hand side of Equation (27) are included into a momentum source term and that equation is then solved as a matrix equation for u .

In the above equations, $\rho' \equiv \rho(1 + \hat{\alpha} C_{VM} \rho_c / \rho)$ is an effective density corrected for virtual mass effects, P is the cell in question, F are the neighbouring cells (6 in a general 3D problem, 4 in 2D), and S'_u is the source term containing all contributions not explicitly written (such as buoyancy and normal turbulent stress terms, for example). $[\Delta p]_P$ and $[\Delta \alpha]_P$ are pressure and void fraction differences evaluated at the cell centre. Note the conservative and consistent formulation of the virtual-mass term, based on the convective coefficients of the other phase (here evaluated with volumetric flow rates). V_P is the volume of a cell, B_P are cell surface areas (evaluated at cell centre P), δt is the time step and u_P^0 is the velocity at the previous time step. For clarity, the phase index was omitted from Equation (27) (it should be assumed in all terms) and so two momentum equations like Equation (27) will exist for the two phases.

It is important to note that the volume fraction appearing in the denominator of the dispersion term, that multiplied by the \mathcal{A} coefficient, is evaluated as an average value over the cell P , thus $\bar{\alpha}_P = \sum_f \alpha_f$. Here α_f are linearly interpolated cell face values and the face index f varies from 1 to 4 in 2D, and 1 to 6 in 3D. In this way the problematic situation of overflow when $\alpha \rightarrow 0$ is prevented.

Convection fluxes at a cell face (f , between P and F) are evaluated with face velocities \tilde{u}_f defined from a special Rhie–Chow interpolation practice [2, 12], as

$$\begin{aligned} \bar{\alpha}_P \tilde{u}_f &= \overline{\sum_F a_F u_F} - B_f [\Delta p]_f - V_f \bar{\mathcal{A}}_f \frac{[\Delta \alpha]_f}{(\bar{\alpha}_P)_f} + \bar{\alpha}_f \bar{C}_f \hat{u}_f V_f \\ &+ \left(\frac{\rho' V}{\delta t} \right)_f \tilde{u}_f^0 + \bar{S}'_u \end{aligned} \quad (30)$$

where the overbar denotes arithmetic average; the virtual-mass term is embedded into the source term S'_u . Note that the gradient of α is evaluated directly at the cell face f (and not by averaging), $[\Delta \alpha]_f = \alpha_F - \alpha_P$, and thus oscillations in α will be avoided.

3.2. Bounding of α and the various forms of the continuity equation

The volume fractions are obtained from solution of one of the continuity equations, either Equation (19) or (20). The important question is how to ensure boundedness of α , i.e. $0 \leq \alpha_k \leq 1$ for $k = c$ or d . Early studies of this issue are found in Carver [13].

3.2.1. Standard method. One of the continuity equations, typically that for the dispersed phase Equation (20), is discretized and solved as a transport equation for $\alpha \equiv \alpha_d$. This equation

is written in the linearized form

$$a_p^\alpha \alpha_p = \sum_F a_F^\alpha \alpha_F + S_\alpha \quad (31)$$

with coefficients and source terms given by (a dispersed phase index is implied):

$$\begin{aligned} a_F^{+\alpha} &= -F_{f^+}^- & a_F^{-\alpha} &= +F_{f^-}^+ & (F^+ \equiv \text{Max}(F, 0), F^- \equiv \text{Min}(F, 0)) \\ a_p^\alpha &= \sum_F a_F^\alpha + \frac{V}{\delta t} + (\nabla \cdot \mathbf{u})^+ \\ S^\alpha &= -(\nabla \cdot \mathbf{u})^- \alpha_p^0 + \frac{V}{\delta t} \alpha_p^0 \end{aligned} \quad (32)$$

A positive cell neighbour or cell face is here denoted F^+ or f^+ (e.g. east, north and top, for the usual compass notation [11]), and a negative cell neighbour and face by F^- and f^- (e.g. west, south and bottom). In arriving at Equations (32), the upwind scheme was used to represent the convective fluxes and the area-velocity products are defined as $F_f \equiv (B\tilde{u})_f$ where B_f is a cell-face area. The other phase volume fraction is then obtained from Equation (21), $\alpha_c = 1 - \alpha_d$. A consequence of upwinding is that all coefficients in Equation (32) are positive so this method guarantees that α_d is bounded by zero ($\alpha_d \geq 0$) but does not guarantee boundedness by 1. Higher order methods are also possible, and in fact are desirable to improve the accuracy of the predicted volume fraction field and alleviate the problems introduced by the numerical diffusion associated with upwinding. These methods should be implemented along the spirit of the high resolution schemes (see e.g. Reference [14]) to guarantee boundedness and, therefore, conclusions similar to those valid for the upwind scheme will hold.

3.2.2. Two-equation method. With this approach both phase continuity equations are solved separately for the two phase fractions. Since it is easy to bound both volume fractions from below ($\alpha_d \geq 0$ and $\alpha_c \geq 0$) using the standard discretisation schemes with the upwind scheme (or a high resolution scheme), and since $\alpha_d + \alpha_c = 1$, then both α_d and α_c will be bounded by 1 at convergence. In order to exactly enforce this constraint, the volume fractions obtained from solution of Equations (19) and (20), denoted α_d^* and α_c^* , are corrected by a factor f as

$$\alpha_d = f\alpha_d^* \quad \text{and} \quad \alpha_c = f\alpha_c^* \quad (33)$$

Now, since $\alpha_d + \alpha_c = 1$, hence

$$f = 1/(\alpha_d^* + \alpha_c^*) \quad (34)$$

Spalding [3] used a similar correction in early developments of his IPSA method but appear to have abandoned it later. A minor point against this method is that it requires solution of two continuity equations. However, due to upwinding, these equations are extremely easy to solve and often one iteration of the CGS solver is sufficient to reduce the initial residuals to below 0.5%. A second point is that the process is iterative in nature with convergence only attained as $f \rightarrow 1$. This is not an issue in steady state calculations where iteration is utilized, and is only a consideration in time-dependent applications.

4. RESULTS

The reformulated momentum equations of Section 2 and the new method for obtaining the volume fractions discussed in Section 3 have been implemented in a computer code. This code is the same used in previous work [2] and is based on the finite-volume method in non-staggered meshes. We can then compare the numerical behaviour of the ‘new formulation’ (that explained in the previous sections) against the ‘old formulation’ (that of Reference. [2]), especially in terms of convergence rate, robustness with mesh refinement, and capacity to handle a wide range of volume fractions in a given problem. In the old formulation the virtual mass term was not included. This term is not problematic numerically but, in order to have a comparison as fair as possible, the virtual mass term is switched off in the new formulation by setting $C_{VM} = 0$ for the test cases in which the two formulations are run side by side.

The following three test cases have been considered:

- (1) Turbulent bubbly flow in an axisymmetric sudden expansion
- (2) Turbulent high-void fraction bubbly flow about a plane obstruction
- (3) Stratified laminar flow in a channel

4.1. Sudden expansion

The relevant dimensions for this problem were $R_1 = 25$ mm, $R_2 = 50$ mm (expansion ratio $R_2/R_1 = 2$), inlet pipe length $L_1 = 25$ mm and outlet pipe length $L_2 = 350 + 1000 = 1350$ mm (first section of length 350 mm was used to concentrate the mesh near the expansion). The flow was turbulent, with $Re = \rho_c 2R_1 P \bar{u}_{c1} / \mu_c \approx 10^5$, and the inlet profiles for both the continuous (liquid) and dispersed (gas) phases were obtained from the measurements of Bel Fdhila [15]. The average value of the void fraction α at inlet was $\approx 5\%$ and the bubble diameter $d_p = 2$ mm. In the experimental arrangement the flow was vertically upwards which we take as direction x (along the pipe axis) and so the only non-zero component of the gravitational acceleration is $g_x = -9.8$ m/s².

4.1.1. Mesh refinement. Three meshes have been utilized, refined consistently (mesh doubling) along both the axial and radial directions. Since the mesh is non-uniform in the axial direction with higher concentration of cells closer to the expansion plane, doubling the mesh requires taking the square-root of the geometrical expansion factors used to distribute the mesh spacing ($f_x \equiv \delta x_{i+1} / \delta x_i$). In this way, the minimum spacing in a zone of non-uniform mesh is effectively halved when going from a coarser to a finer mesh. The mesh characteristics are given in Table I, where f_x refers to the mesh blocks (length 350 mm) just downstream of the expansion plane.

An idea of the finer mesh (mesh-3) can be obtained from Figure 1, where contours of the predicted void fraction (α) and turbulent kinetic energy (normalized by its maximum value) are also given, together with the mixture streamlines. These are evaluated by adding the liquid and the gas volumetric flow rates across a cell face, and summing the contributions for each cell face from the axis of symmetry ($r=0$) to the desired radial position (r_j), thus $\Psi_{M_j} = \Psi_{M_{j-1}} + (\alpha_c \tilde{u}_{cj} B_{fj}) + (\alpha_d \tilde{u}_{dj} B_{fj})$ (j denotes a position along the radial direction and B_{fj} the corresponding cell face area). The streamfunction for the two-phase mixture Ψ_M is then normalized by the total (liquid plus gas) inlet flow rate and

Table I. Meshes used for the sudden expansion case (NC: number of cells; δx : cell size; f_x and f_r : mesh expansion factors).

Mesh	NC	$\delta x_{\min}/R_1$	f_x	f_r
1	2200	0.1	1.01560	1.0
2	8800	0.05	1.00770	1.0
3	35200	0.025	1.00384	1.0

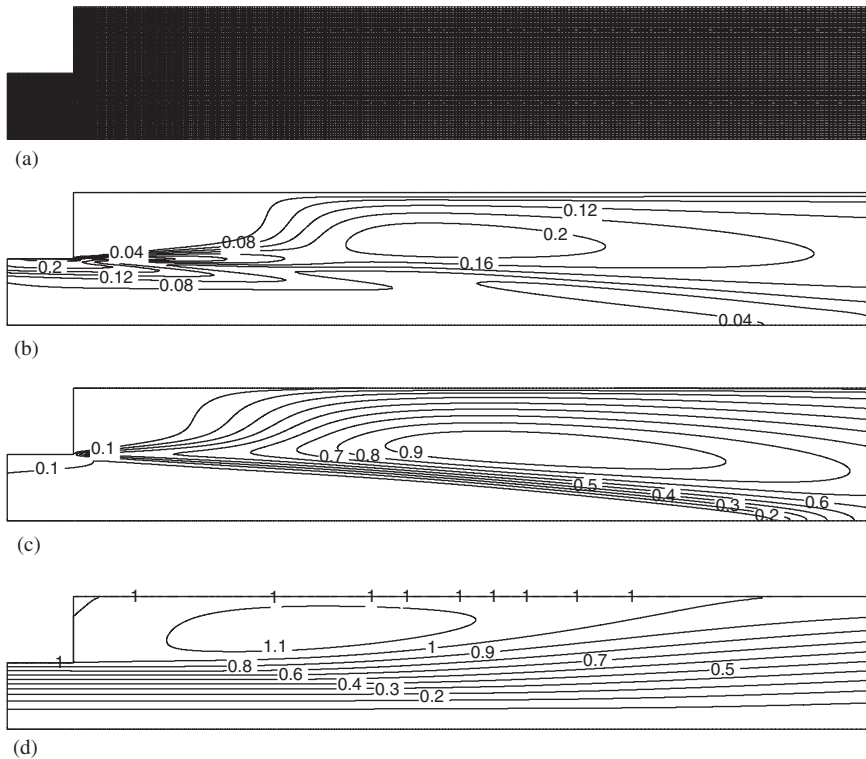


Figure 1. Predictions for the sudden expansion flow (flow is left to right, with gravity in the opposite direction): (a) mesh, (b) void fraction contours, (c) turbulent kinetic energy contours, and (d) mixture streamlines.

is arbitrarily set to zero at the symmetry axis. Figure 1 shows agglomeration of the gas phase in the main part of the recirculating zone, where the turbulent kinetic energy also shows its highest levels. The region just behind the step-wall is devoid of gas bubbles ($\alpha \approx 0$).

The effect of mesh refinement upon the predicted profiles of void fraction is shown in Figure 2. There is good convergence with mesh refinement except for the profile closer to the expansion plane ($x = 70$ mm) where larger differences are seen in the predictions with the coarser mesh (the local maximum of α at $r/R_1 \approx 0.7$ is due to the imposed inlet profile).

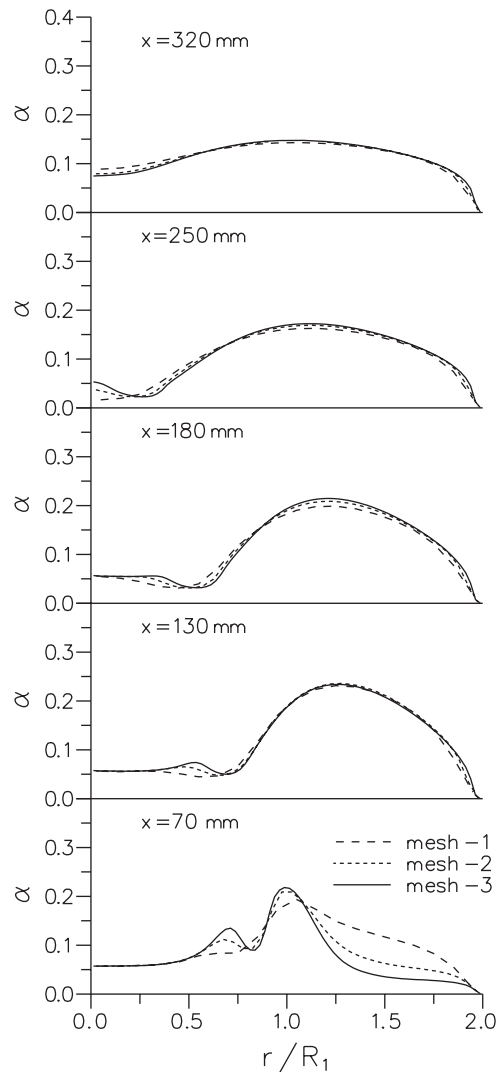


Figure 2. Effect of mesh refinement on the void fraction profiles.

4.1.2. New and old formulation. The main differences between the two are the division of the momentum equations by α and the inclusion of the virtual mass term. The division by α implies some difference on the stress terms (due to the approximation $\tau_{ki} = \tau_k$; compare Equation (2) with Equation (8)). In practice, the ‘old formulation’ solves the equations with a stress (molecular plus turbulent) divergence term written as $\nabla \cdot (\alpha \tau)$, therefore assuming that the interfacial stress vanishes, while in the ‘new formulation’ the term is $\alpha \nabla \cdot \tau$, on the assumption that the interfacial stress is equal to the bulk phase stress. In terms of the method used to obtain α , the ‘old formulation’ uses the standard method (Section 3.2.1) while the

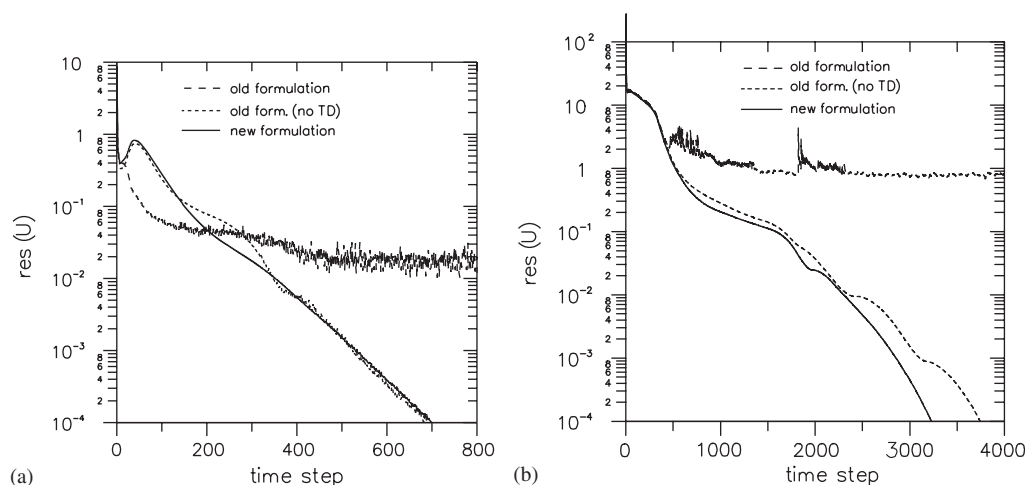


Figure 3. Decay of the residuals with the 'old' and the 'new' formulations. The old formulation converges only when the turbulent drag (TD) term is switched off. (a) Calculations on mesh-1; (b) calculations on mesh-3.

'new formulation' can use either of two methods (Sections 3.2.1 and 3.2.2) for solving the α -equation. This choice does not entail any significant difference upon the solution, as will be shown later.

For the predictions on the coarser and the finer meshes, Figures 3(a) and 3(b), respectively, show the decay of the u -momentum residuals as time-marching proceeds (the behaviour of the other variables is similar). The figure compares the residuals' history with the two formulations, and also with the old formulation when the turbulent-drag term in the dispersed phase momentum equation is switched off (second term in Equation (5)). Clearly, when this term is present the old formulation cannot converge to the specified tolerance (here 10^{-4}) but by switching it off convergence can be achieved. The results without the turbulent-drag term do exhibit, however, a much reduced level of bubble dispersion.

In the new formulation all terms are present and no convergence problems arise. This problem with the old formulation was traced back to the relative velocity which attains unphysical high values just inside the area where $\alpha_d \approx 0$ because the momentum equation is then singular (or undefined $0=0$). The drag function C_f in the turbulent-drag term contains the relative velocity (cf. Equation (5)) and because that term is not multiplied by α_d , it will become troublesome for iterative convergence. For this case the problem is restricted to a few problematic cells in that area.

A few comparison of volume fraction profiles obtained with the new and old formulations (using the same method for α) are shown in Figure 4(a) for mesh-1 and Figure 4(b) for mesh-3 (the finest). The differences seen in these figures are a result of the approximation $\tau_{ki} = \tau_k$; they are small and only become significant close to the expansion plane. In terms of mean velocities the differences are even smaller, as shown in Figure 4(c) where profiles of the axial velocity component for the continuous phase, obtained on mesh-3 at the same locations as before, are compared.

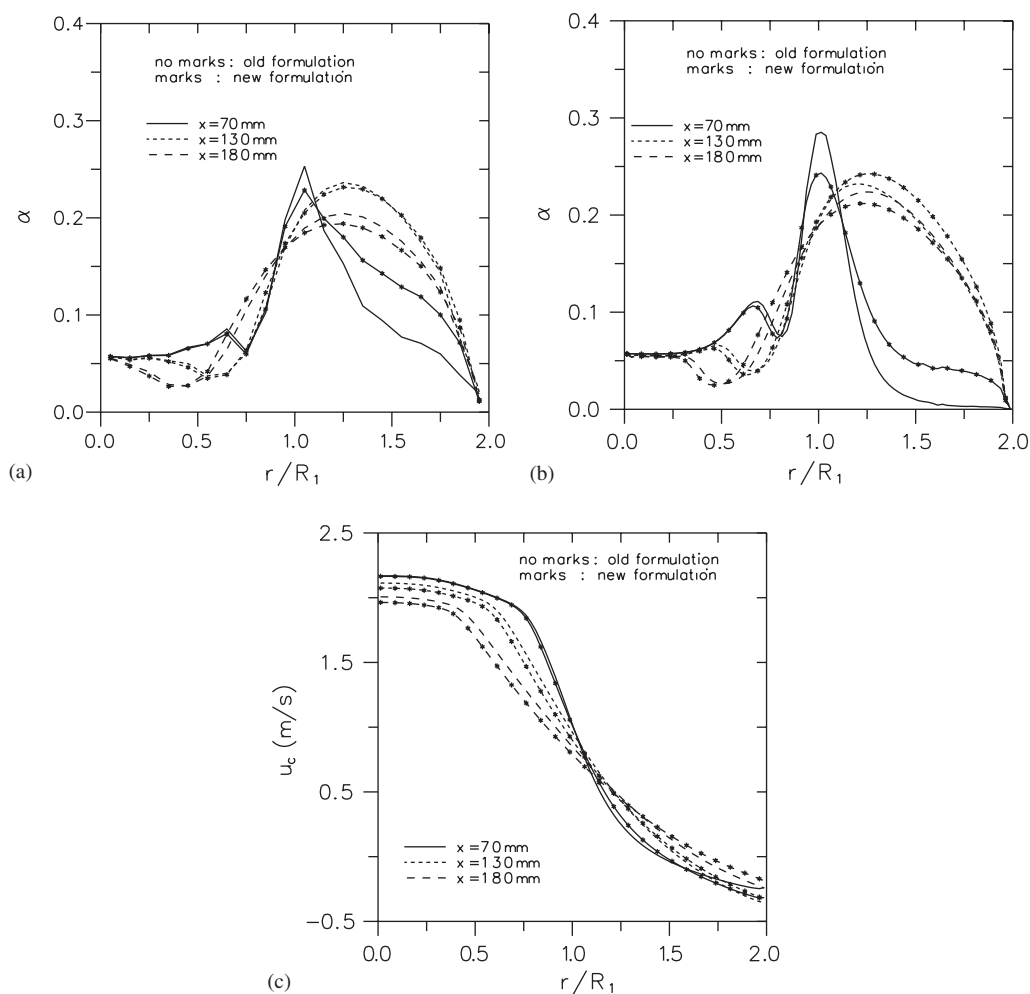


Figure 4. Comparison of three profiles predicted with the 'new' and the 'old' formulations. Void fractions based on the standard method. (a) Void fraction on the coarse mesh (mesh-1); (b) Void fraction on the finest mesh (mesh-3); (c) Axial velocity of continuous phase on the finest mesh (mesh-3).

4.1.3. Bounding of volume fraction and method used to solve for α . In terms of accuracy, Figure 5 shows three typical radial profiles of α predicted on mesh-2 with the standard and the two-equation method; both give essentially the same results.

In terms of robustness the various methods are applied to solve for α_c , instead of α_d , since in this way the more problematic bounding from above ($\alpha \leq 1$) can be assessed with this flow problem (due to the region where $\alpha_d = 0$). The results are summarized in Table II which gives the number of time steps to convergence (tolerances of 10^{-4} and 10^{-5}) and cpu times.

As expected, the two-equation method requires somewhat higher execution times compared with the existing (more 3.9% on the coarse mesh and 4.0% on the fine mesh). However, on the fine mesh it performs very well, converging in the same number of time steps as

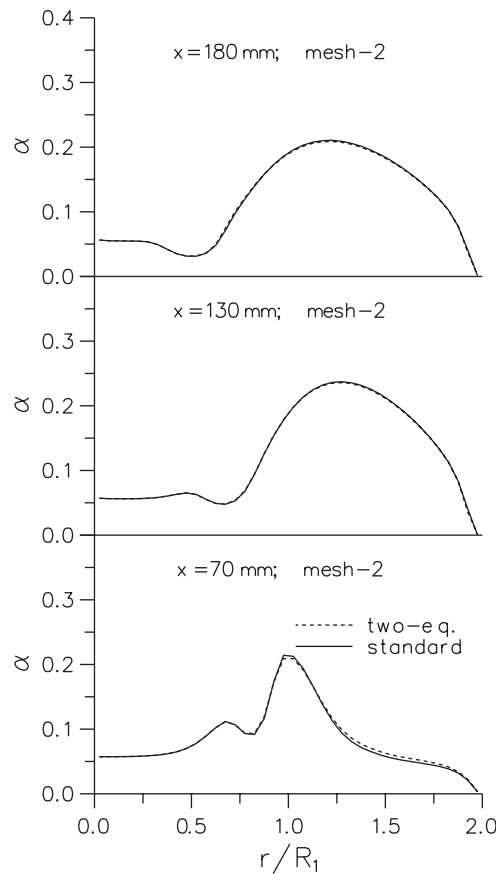


Figure 5. Effect on the predictions of the method used to obtain the volume fractions. Calculations on the medium mesh (mesh-2).

Table II. Number of time steps and CPU times (sec) (given in parenthesis) for convergence with the two bounding schemes for the sudden expansion.

Method	Solve for:	Mesh-1, Tol = 10^{-4}	Mesh-1, Tol = 10^{-5}	Mesh-3
Standard, 3.2.1	α_d	698 (47.2)	815 (54.1)	3766 (8686)
	α_c	762 (60.0)	> 10000(640)	> 10000
Two-equations, 3.2.2	α_d	698 (49.1)	815 (56.2)	3767 (9166)
	α_c	698 (49.1)	815 (56.2)	3767 (9166)

the standard method when solving for α_d (when no upper bounding of α_d is necessary). The standard method fails to converge on the finer meshes when solving for α_c , the two-equation method on the other hand performs identically well since it solves for both α_c and α_d .

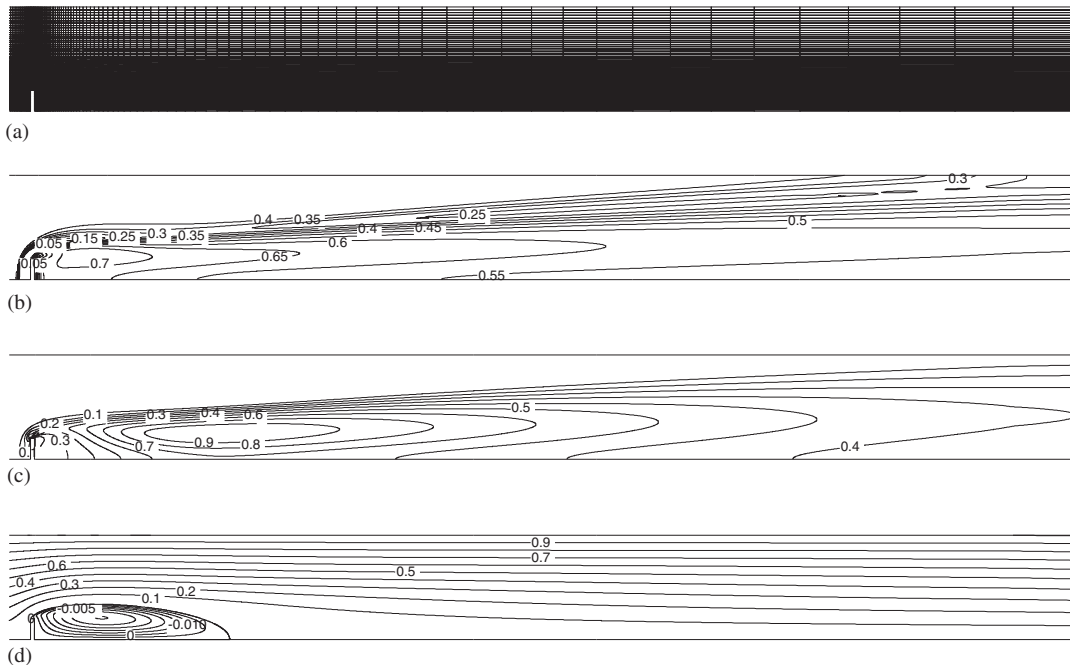


Figure 6. Predictions for the flow around an obstruction (flow is left to right and there is no gravity): (a) mesh, (b) void fraction contours, (c) turbulent kinetic energy contours, and (d) mixture streamlines.

4.2. Flow around obstruction

In this problem a high void-fraction (inlet $\alpha = 40\%$), two-dimensional, turbulent, air/water mixture flows in the absence of gravity around a planar obstruction in a channel (blockage ratio $H_2/H = 5$, where H_2 is the half-width of the channel and the half-width of the obstruction is $H = 10$ mm; see Figure 6(a)). This flow resembles that around impeller blades where large zones of high void fraction are generated. The region in front of the obstruction ($x \leq 0$) is devoid of bubbles (high pressure region) and the region behind the obstruction ($x > 0$) has considerable bubble concentration but α is still far from 1 ($\alpha_{\max} \approx 74\%$). Due to this, the matter of bounding α by 1 was studied indirectly by solving the equation for α_c (which is 1 at the start of the calculations, and is also 1 in the high-pressure region of the final steady-state solution, thus posing bounding problems).

Uniform inlet profiles for volume fraction ($\alpha_d = 0.4$) and velocity ($u_c = 2$ m/s, $u_d = 2.2$ m/s) were imposed at the entrance plane at $x = -L_1$ ($L_1 = 250$ mm). The thickness of the obstruction was 2 mm and the region downstream was $L_2 = 500$ mm long. The absence of gravity leads to an increase in bubble concentration behind the obstacle.

4.2.1. Solution fields and mesh refinement. The meshes used are summarized in Table III and a portion of the fine mesh is given in Figure 6(a). The predicted fields obtained on mesh-2 are shown for void fraction in Figure 6(b), and turbulent kinetic energy (normalised with its

Table III. Characteristics of meshes used for the obstruction problem (NC-number of cells; δx_{\min} : minimum cell size; f_x and f_y : expansion factors ($f_x \equiv \delta x_{i+1}/\delta x_i$).

Mesh	NC	$\delta x_{\min}/H$	$f_{x-\max}$	$f_{y-\max}$
1	3270	0.05	1.1295	1.0607
2	13080	0.025	1.0628	1.0299

maximum value, $0.370 \text{ m}^2/\text{s}^2$) in Figure 6(c), and mixture streamlines in Figure 6(d). The most striking feature is the zone in front of the obstacle where the void fraction falls sharply from 40% to zero. There is accumulation of bubbles behind the obstacle, in the recirculating zone which extends up to $X_R/H = 8.27$ and also in the area of high turbulence kinetic energy which develops in the shear layer behind the recirculation zone.

Several lateral profiles of void fraction are shown in Figure 7 for the two computational meshes. More mesh refinement would be required for the profiles closer to the obstacle (namely at $x/H = 0.5$ and 1) to be less sensitive to the mesh, whereas those further downstream show little differences for the these two meshes.

4.2.2. Bounding of volume fraction and equation used for α . The effect of the equation used to solve for α on the accuracy of the results can be seen from Figure 8. This figure compares predictions of void fraction obtained with the standard (Equation (20)) and the two-equation (Equations (33)–(34)) methods on the fine mesh, at two locations upstream of the contraction ($x/H = -0.5$ and -0 , just upstream of the obstacle) and two locations downstream. No differences can be distinguished in the figure. A comparison of the α variation along the centreline also show a lack of effect, with both methods predicting an identical recirculating zone behind the obstruction, extending to a distance of $8.27H$.

We examine now the relation between bounding method and robustness. The number of time steps for convergence (to a tolerance of 10^{-4}) are given in Table IV, as well as the corresponding CPU times in seconds (in a DEC-10000 machine). In all cases the time step was fixed at $\delta t = 5 \times 10^{-4} \text{ s}$ which gives an approximate local Courant number of 3.1 on mesh-1 and 6.2 on mesh-2.

Table IV shows that the standard method fails to converge on both meshes when solving for α_c . The two-equation method does very well on either mesh and its performance matches that of the standard method when the latter solves for α_d .

4.3. Phase stratification in a channel

The development of stratification of gas and liquid laminar flow is examined in a 2-D channel of width $H = 10 \text{ mm}$ and length $L = 100 \text{ mm}$ ($L/H = 10$). The density difference between the two phases was chosen to be small ($\rho_c = 1000 \text{ kg/m}^3$ and $\rho_d = 950 \text{ kg/m}^3$) so as to minimize numerical problems related to large discontinuities in pressure gradient at the interface. The other properties have been carefully chosen to guarantee adequate development of the flow from the inlet condition of the two equally mixed phases ($\alpha_d = 0.5$), to a complete stratification. Since the pressure drop is inversely proportional to the Reynolds number and should be approximately equal in both phases, one should have $\rho_c \bar{u}_c / \mu_c = \rho_d \bar{u}_d / \mu_d$. The viscosities of the two phases were $\mu_c = \mu_d = 10^{-3} \text{ Pa s}$ and the diameter of the ‘bubbles’ $d_p = 2 \text{ mm}$, thus

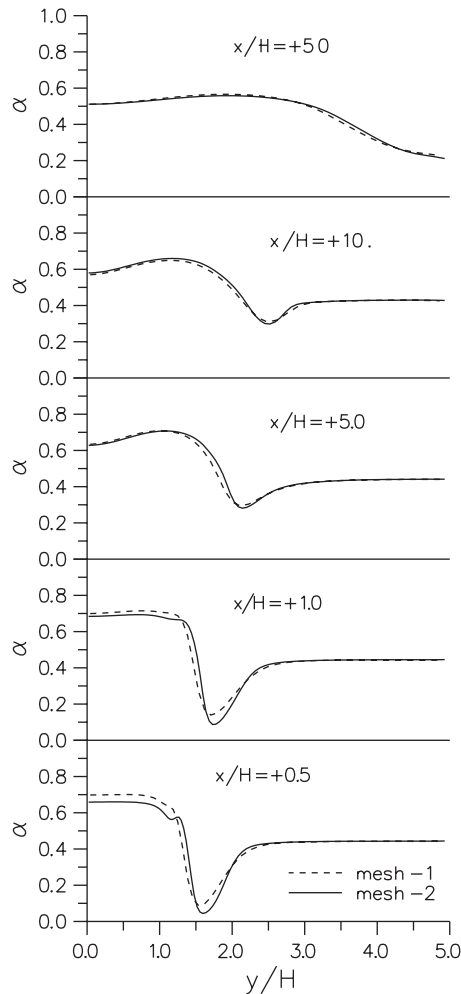


Figure 7. Effect of mesh refinement on the void fraction variation. Void fraction based on the two-equation method.

implying a terminal velocity of $u_{r0} = 0.0307$ m/s. The inlet velocities of $\bar{u}_{c-inl} = 0.1$ m/s and $\bar{u}_{d-inl} = 0.105$ m/s give $Re = 1000$ and the different time scales of the flow are: relaxation time $t_p = 0.0909$ s; relative or settling time $t_r = H/u_{r0} = 0.326$ s; diffusion time $t_D = H^2/\nu_c = 100$ s; convective time $t_C = L/\bar{u}_{c-inl} = 1$ s.

4.3.1. Solution fields and mesh refinement. Two uniform meshes with 50×20 and 100×40 cells have been utilized. The development of the lighter phase distribution is shown in Figure 9 (using the two-equation method). At the stations $x = 1$ and $2 H$ from inlet, the imposed inlet volume fraction of 0.5 is still seen in the central portion of the channel, but further downstream the two phases have fully separated with the heavier phase flowing at the

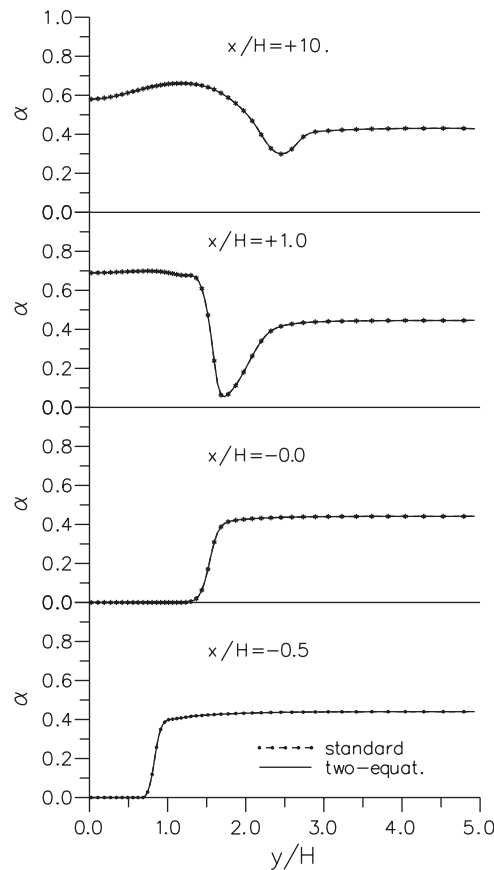


Figure 8. Effect of the equation solved for α on the predicted void fraction. Calculations on the finest mesh (mesh-2).

Table IV. Number of time steps and cpu-time for convergence with the two bounding schemes (obstruction flow problem).

Method	Solve for:	Mesh-1	Mesh-1	Mesh-2	Mesh-2
		Time steps	cpu (s)	Time steps	cpu (s)
Standard	α_d	3635	380	4230	2408
	α_c	> 10000	> 1060	diverge	—
Two-equations	α_d	3615	345	4257	2547
	α_c	3615	345	4257	2547

bottom ($\alpha_d = 0$ for $y/H < 0.5$) and the lighter at the top ($\alpha_d = 1$ for $y/H > 0.5$). The slight over/undershoots of α in the first profiles are due to the problems arising from the Rhie–Chow interpolation.

The predictions in Figure 9 are based on the finer mesh of 100×40 cells. With the coarser mesh (50×20 cells) the sharp interface between the regions of $\alpha_d = 0$ and 1 is less well

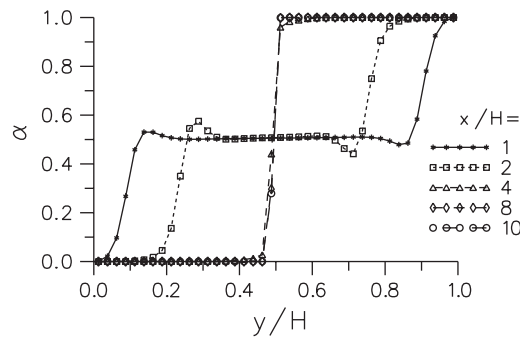


Figure 9. Profiles of void fraction at several stations along the channel. Calculations on the fine mesh and based on the two-equation method.

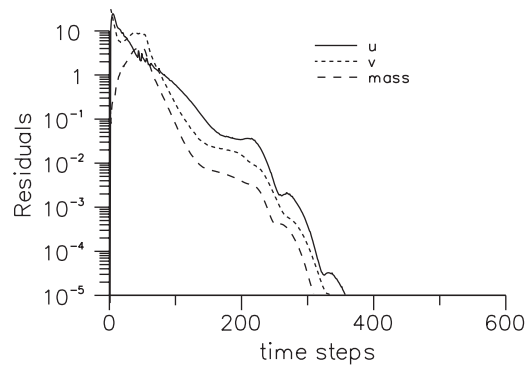


Figure 10. Residuals history with two-equation method on the fine mesh.

resolved, otherwise most other features are unchanged. For the profile near outlet ($x/H = 10$) the interface is resolved in 2 cells with the fine mesh.

4.3.2. Effect of bounding scheme. Figure 10 shows the convergence history for several equation residuals: axial and radial momentum (u_c and v_c), and overall (gas plus liquid) mass conservation. These show good convergence behaviour, while the standard method fails altogether because of the effect of phase segregation.

5. CONCLUSIONS

The division of the momentum equations for each phase by the corresponding volume fraction seems to lead to better convergence characteristics of the two-phase flow algorithm. This improved numerical stability is retained with refinement of the computational meshes (very fine meshes were used in the two-dimensional test problems here presented). Some related *physical* issues should be further investigated (e.g. should the stress term in the equations be $\nabla \cdot \alpha \tau$ or $\alpha \nabla \cdot \tau$).

The two-equations bounding scheme, which solves the continuity equations for both phases, showed excellent overall behaviour easily coping with extreme cases of fully segregated phases.

ACKNOWLEDGEMENTS

The work was performed as part of Brite Project BE 4322. P.J. Oliveira wishes to thank Fundação para a Ciência e Tecnologia (FCT), Portugal, for receipt of sabbatical grant No. FMRH/BSAB/68/98.

REFERENCES

1. Crowe CT, Sommerfeld M, Tsuji Y. *Multiphase Flow with Droplets and Particles*. CRC Press: Boca Raton, 1998.
2. Issa RI, Oliveira PJ. Numerical prediction of phase separation in two-phase flow through T-junctions. *Computers and Fluids* 1994; **23**:347–372.
3. Spalding DB. The numerical computation of multi-phase flows. CFDU, Imperial College, London, *Report CFD/85/7*, 1985.
4. Kunz RF, Siebert BW, Cope WK, Foster NF, Antal SP, Ettorre SM. A coupled phasic exchange algorithm for three-dimensional multi-field analysis of heated flows with mass transfer. *Computers and Fluids* 1998; **27**:741–768.
5. Wu J-C, Minemura K. Numerical prediction of turbulent bubbly two-phase flow in a rotating complicated duct. *International Journal for Numerical Methods in Fluids* 1999; **29**:811–826.
6. Issa RI, Oliveira PJ. Numerical prediction of turbulence dispersion in two-phase jet flows. In *Two-Phase Flow Modelling and Experimentation*. 1995, Celata GP, Shah RK (eds). Edizioni ETS: Italy, 1995; 421–428.
7. Issa RI, Oliveira PJ. Assessment of a particle-turbulence interaction model in conjunction with an Eulerian two-phase flow formulation. In *Turbulence, Heat and Mass Transfer*, Hanjalic K, Peeters TWJ (eds), vol. 2. Delft Univ. Press: Delft, 1997; 759–770.
8. Tomiyama A, Matsuoka T, Fukuda T, Sakaguchi T. A simple numerical method for solving an incompressible two-fluid model in a general curvilinear coordinate system. In *Advances in Multiphase Flow*, Serizawa A, Fukano T, Bataille J (eds). Elsevier: Amsterdam, 1995; 241–252.
9. Harlow FH, Amsden AA. Flow of interpenetrating material phases. *Journal of Computational Physics* 1975; **18**:440–464.
10. Spalding DB. A turbulence model for buoyant and combusting flows. *International Journal for Numerical Methods in Engineering* 1987; **24**:1–23.
11. Patankar SV. *Numerical Heat Transfer and Fluid Flow*. Hemisphere Pub.: Washington, DC, 1980.
12. Oliveira PJ. Computer modelling of multidimensional multiphase flow and application to T-junctions. *PhD Thesis*, Imperial College, 1992.
13. Carver MB. A method of limiting intermediate values of volume fraction in iterative two fluid computations. *Journal of Mechanical Engineering Science* 1982; **24**:221–224.
14. Leonard BP. Bounded higher-order upwind multidimensional finite-volume convection–diffusion algorithms. In *Advances in Numerical Heat Transfer*, Minkowycz WJ, Sparrow EM (eds), vol. 1. Taylor & Francis, London, 1996; 1–57.
15. Bel Fdhila R, Simonin O. Eulerian prediction of a turbulent bubbly flow downstream of a sudden pipe expansion. In *Proceedings of the 6th Workshop on Two Phase Flow Predictions*, Sommerfeld M (ed), University of Erlangen, 1992.